Microparticles in a deep ice core drilled at NEEM, Greenland: cryogenic scanning electron microscopic observations of location, size, shape, and constituent elements

Wataru SHIGEYAMA[1,2]*, Fumio NAKAZAWA[1,2], Kumiko GOTO-AZUMA[1,2],

Tomoyuki HOMMA[3], Naoko NAGATSUKA[2], Ramona V. MATEIU[4],

Morimasa TAKATA[3], Nobuhiko AZUMA[3] and Dorthe DAHL-JENSEN[5,6]

[1] Department of Polar Science, The Graduate University for Advanced Studies, SOKENDAI, 10-3 Midori-cho, Tachikawa, Tokyo 190-8518.

[2] National Institute of Polar Research, 10-3 Midori-cho, Tachikawa, Tokyo 190-8518.

[3] Nagaoka University of Technology, 1603-1 Kamitomioka-machi, Nagaoka, Niigata 940-2188.

[4] Department of Chemical and Biochemical Engineering, Technical University of Denmark, Kgs Lyngby 2800, Denmark.

[5] Centre for Earth Observation Science, University of Manitoba, 535 Wallace Building, Winnipeg, MB R3T 2N2, Canada.

[6] Physics of Ice, Climate and Earth, Niels Bohr Institute, University of Copenhagen, Tagensvej, 16, 2100 Copenhagen OE, Denmark.

*Corresponding author: Wataru Shigeyama (w.shigeyama@gmail.com,

present address: JEOL Ltd., 1-2 Musashino, 3-Chome Akishima, Tokyo 196-8558.)

(Received March 31, 2021; Accepted August 26, 2021)

Abstract: This report presents the analysis of microparticles contained in the deep ice core drilled at the North Greenland Eemian Ice Drilling (NEEM) site, using a cryogenic scanning electron microscope (SEM) equipped with an energy dispersive X-ray spectrometer (EDS). By implementing additional optical microscopic analysis prior to cryogenic SEM/EDS analysis, it was possible to exclude artifacts formed during the cryogenic SEM/EDS experiments. The examined ice core samples

were cut from depths corresponding to five different climate stages, from the Holocene period through the last interglacial epoch. Overall, 514 microparticles were observed via SEM, and 151 of those were also analyzed based on their EDS spectra to determine their chemical compositions. A catalog containing the details of all the observed microparticles was then constructed. The catalog presents optical and secondary electron images of microparticles, an area-equivalent diameter and aspect ratio of each microparticle, and its distance from the nearest grain boundary and air-inclusion (i.e., air bubble, hydrate) or plate-like inclusion. For microparticles analyzed with EDS, numerical data regarding the X-ray count, weight ratio, and atomic ratio are also included, and the atomic ratio is shown as a pie chart. In this report, we describe how the observations and analyses were carried out and how the catalog data were organized. The catalog is valuable for studies regarding the general paleoenvironment and the relationship between microparticles and the physical properties of ice in polar ice sheets.

1. Background and Summary

Microparticles (hereafter, particles) within ice sheets affect the physical properties of the ice, including its grain size, crystal orientation fabric, and the recrystallization of ice crystals[1,2]. The physical properties of ice, and possibly the particles themselves, strongly impact ice deformation[1,3,4], and therefore influence ice sheet/glacier flow. Particles in ice cores retrieved from ice sheets provide a variety of paleoenvironmental proxies[5–10] and serve as useful tools for investigating their impacts on radiative forcing[11,12] and biogeochemical cycles[13]. Extensive studies have been carried out to document variations in concentrations and sizes of particles in ice cores[5–8,10,14,15]. Both soluble and insoluble particles are contained in ice sheets. Insoluble particles are usually measured in melted ice core samples by a Coulter counter[14] or a laser particle counter[15]. Most of the insoluble particles have been assumed to originate from mineral dust[6,14,15], while soluble ones such as $CaCO_3$, $NaCl$, $CaSO_4$, and Na_2SO_4 particles originate from mineral dust, sea-salts, or chemical reactions of $CaCO_3$ or $NaCl$ with H_2SO_4[16,17]. By melting ice samples, it is neither possible to analyze chemical compositions of individual soluble particles nor observe the locations, sizes, or shapes of soluble and insoluble particles, although dissolved soluble particles in melted samples can be usually measured as ions by ion chromatography[15,16]. However, chemical compositions of individual soluble particles can provide invaluable information on sources, transport processes including chemical reactions during transport, and deposition onto ice sheets[8,18]. Sizes and shapes of particles (both soluble and insoluble) and

locations of particles relative to grain boundaries are important because they can affect grain boundary migration and recrystallization[2,19,20], which affect mechanical properties of ice[1,2]. The locations of the particles relative to air-inclusions[21] (bubbles or hydrates) or plate-like inclusions[22] (PLI) are also important because particles can affect nucleation and annihilation of the inclusions, which would be related to preservation of atmospheric gases in ice cores[23]. It is therefore essential to document the locations (i.e., distances from grain boundaries and distances from air-inclusions or plate-like inclusions), sizes, shapes, and constituent elements of both soluble and insoluble particles in an ice core to understand their impacts on the physical properties of the ice and to extract detailed information regarding the past environment.

Micro-Raman spectroscopy[24–26] and energy dispersive X-ray spectroscopy (EDS) used in combination with cryogenic scanning electron microscopy (SEM)[27] have been employed for in situ observations of particles in non-melted ice core samples. Specifically, micro-Raman spectroscopy can be used to analyze the locations and chemical forms of particles. However, a large proportion of the particles in ice sheets are smaller than 1 μm[14,28], and this technique cannot be used to evaluate the sizes or shapes of particles <1 μm because of the spatial resolution limits of optical microscopy (OM). Additionally, although NaCl is one of the most common impurities in polar ice cores, it is difficult to detect NaCl due to its weak Raman signal[26].

The cryogenic SEM instrument used in this work was equipped with a cold stage, which maintained ice samples at a low temperature. Using cryogenic SEM with an EDS detector, it is possible to investigate the locations, sizes, shapes, and constituent elements of particles <1 μm contained in the ice[27]. However, in situ studies of particles using cryogenic SEM/EDS are relatively rare because they are very time-consuming[27]. Most reports describing cryogenic SEM/EDS studies have been carried out either after subliming the ice surface in a cold laboratory or while the ice surface was being sublimed under vacuum. During sublimation, impurities located at grain boundaries and in the ice crystal lattice coalesced and formed artifacts so-called "white spots" and "filaments."[29] It has therefore been difficult to differentiate particles originally contained in the ice from those formed during sublimation. To our knowledge, there have been very few observations of the sizes and shapes of originally-contained particles.

This report presents the cryogenic SEM/EDS analyses of particles contained in the deep ice core, drilled as a part of the international North Greenland Eemian Ice Drilling (NEEM) project[30]. With additional OM analysis conducted prior to the cryogenic SEM/EDS analysis, it was possible to exclude

artifacts formed during cryogenic SEM/EDS experiment. Although submicron particles that are unable to be detected with OM were not measured in our study, sizes and shapes of particles with diameters as small as ~1 μm were analyzed, which is not possible with micro-Raman spectroscopy. The ice core samples were cut from depths corresponding to five climate stages including the Holocene period, back through the last interglacial epoch. Overall, 514 particles were investigated using SEM, and for 151 of those particles, EDS spectra were also obtained to examine their chemical components. This allowed the creation of a catalog of all of the observed particles, compiling the optical and secondary electron images, area-equivalent diameters, and aspect ratios of each particle, as well as their distances from the nearest grain boundary, and their distances from the nearest air-inclusion or PLI. For the particles that were also analyzed with EDS, numerical data regarding the X-ray count, weight ratio, and atomic ratio are presented (the atomic ratio is also shown as a pie chart). Herein, we describe how the observations and analyses were carried out and how the catalog data are organized.

2. Location

This study investigated ice core samples drilled as a part of the NEEM project during the years 2008–2012. The drill site is located at 77.45 °N, 51.06 °W, at an altitude of 2450 m above sea level (Fig. S1). The core was drilled down to a depth of 2540 m. The annual mean temperature was –29 °C, and the annual mean surface mass balance was 0.22 m in ice equivalent[30]. The deep ice core goes back 128,500 years before A. D. 1950 (BP).

3. Methods and Technical Validation

Samples were prepared in a cold laboratory. First, the particles in each sample were observed with an optical microscope. Then, the same particles were examined using a cryogenic SEM, which enabled measurements of their sizes, shapes, and locations in the ice. Finally, EDS analyses were performed for selected specimens. The detailed procedure is described below.

3.1. Sample preparation

The NEEM deep ice-core was cut into 550 mm-long sections at the drilling location. Each section was placed in a plastic bag, numbered in order, and named using the bag number. In this study, we took samples from five bags (226, 2815, 3575, 3925, and 4375). The upper or lower 110 mm of

the ice in each bag had already been consumed by other analyses. In a cold laboratory (–20 °C) at the National Institute of Polar Research (Tokyo, Japan), we used a bandsaw to cut the remaining ice from each bag into five pieces, labeled A, B, C, D, and E (Fig. 1). We then cut multiple specimens (Fig. 1) from 1–2 pieces of each bag. The length, width, and thickness of each specimen were 4–12 mm, 5–11 mm, and 1–4 mm, respectively.

Next, each specimen was fixed on a holder consisting of a shuttle and an aluminum stub, similar to the setup used by Barnes et al.[31] The details of the method for fixing the specimen are identical to those described by Shigeyama et al.[32] After fixing a specimen on a holder, the ice surface was smoothed using a microtome. For some specimens, the surface that had already been smoothed and analyzed was shaved, and then the particles on the new surface were analyzed. This procedure was repeated one or two more times, such that particles from multiple layers of each specimen were analyzed (Fig. 1). The details of the investigated specimens are listed in Table 1.

3.2. Experimental details

We first identified particles in the ice specimens using an optical microscope (BX 51, with objective lenses LMPLFLN5xBD (x5), LMPLFLN10xBD (x10), or LMPLFLN20xBD (x20); Olympus Corporation, Tokyo, Japan) in a cold laboratory (–20 °C). Next, we examined these particles with an environmental scanning electron microscope (Quanta 450 FEG; Thermo Fisher Scientific, Inc., Materials and Structural Analysis Division, Hillsboro, OR, USA) equipped with a cryogenic preparation system (PP3010; Quorum Technologies, Lewes, UK). Figure 2 illustrates the method for analyzing the particles. In OM images, particles appear darker than the surrounding ice (Fig. 2(a)) and are referred to as "black dots". The particles ranged in size from several μm to tens of μm in a previous study from Eichler et al.[25] The black dots looked brighter than the ice in the cryogenic SEM images (Fig. 2(b)). Importantly, it is possible to observe particles both on the surface and inside the ice, as a result of the wide focusing range of optical microscopy (Fig. 2(c); the depth of focuses are 70 μm, 18 μm, and 6.1 μm for lenses LMPLFLN5xBD, LMPLFLN10xBD, and LMPLFLN20xBD, respectively), whereas only particles on the surface of the ice can be observed with cryogenic SEM (Fig. 2(d)). To investigate the particles inside the ice, each specimen in the SEM chamber was sublimed several times by increasing the temperature of the cold stage from –100 to –50 °C under the low vacuum (chamber pressures of 10, 50, or 120 Pa), This treatment allowed us to make relatively smooth ice surface than that under higher vacuum (i.e., a lower pressure). The total sublimed ice thickness was up to several

tens of micrometers, being mostly several micrometers.

After exposing the particles on the ice surface, it was necessary to suppress the sublimation of the ice specimen and the condensation of frost[32–34]; therefore, the pressure in the SEM chamber was regulated to 10, 50, or 120 Pa using dry nitrogen gas[32]. Under such pressures, backscattered electron images are often used rather than secondary electron images, because secondary electrons are diffused (signals are weakened) by gases in the SEM chamber. However, a secondary electron detector was used in this study because it can acquire an image faster than the backscattered electron detector does for an image with a same resolution. The detector used in this study was a large field detector (SP 4022 268 01384; Thermo Fisher Scientific, Inc., Materials and Structural Analysis Division), which was designed for low-vacuum/environmental SEM. In most cases, the temperature of the cold stage was set to –140 °C, but if necessary, the temperature was changed within the range of –155 to –110 °C to minimize the effect of surface sublimation and frost condensation. The secondary electron images of the particles were obtained at an acceleration voltage of 10–20 kV and a beam current of 0.6–13 nA (spot size = 4–6). For selected specimens, an energy dispersive X-ray spectrometer (X-Max 50; Oxford Instruments, plc, Abingdon, UK) was used to analyze the constituent elements of the particles. The EDS analyses were performed with an energy range of 10–40 keV; 1024, 2048, or 4096 channels; and a spectral resolution of 5–39 eV. The X-ray spectra were acquired for 15 s or until the count reached 300,000 (determined using AZtec® software, Oxford Instruments). The particles as well as the surrounding ice were analyzed, so it was possible to determine whether the elemental signals were derived from the particles by comparing the EDS data for a particle and for the ice (see Sec. 3.5.).

3.3. Measuring the size and shape of particles

The size and shape of each particle were measured based on the secondary electron images. A particle was defined as a closed region that appeared brighter against the dark background (ice) in the secondary electron images. Frost and surface roughness were identifiable from their shape and could therefore be differentiated from the particles. A brighter region where multiple particles aggregated to form a larger particle was considered as a single particle (see Fig. 2(b) inset). When multiple particles existed at the position of a single black dot observed in the OM images, each one was regarded as a separate particle.

To define the outline of each particle, binary image processing was applied to all of the secondary electron images using the image analysis software, Image J (Image J v1.52a or Fiji v1.52p)

or Python-OpenCV (Python v3.8.1 or v2.7.15; OpenCV v4.1.2 or v3.4.3), depending on the computers we used. The types of software differed on the three computers we used. The measurements performed by binarization with Image J were described as α, and those with Python-OpenCV were described as β in the catalog (Fig. 3). If the processing could not differentiate the particle and the surrounding ice well, the outline was drawn manually (Fig. 3).

From the outline, it was possible to calculate an area-equivalent diameter and an aspect ratio. The area-equivalent diameter is the diameter of a circle that has the same area as the outlined shape of the particle. The aspect ratio is the ratio of the minor-axis length to the major-axis length of the area-equivalent ellipse. By definition, the aspect ratio lies between 0 (flat) and 1 (a square or a perfect circle). The Image J software was used to calculate the sizes and aspect ratios of all particles. Binarization by Image J and Python-OpenCV gave differences in diameter of about 1%, and no difference in the aspect ratio. Repeated measurements by manual outline drawing gave differences in diameter of about 7%, and 0.1 in the aspect ratio.

3.4. Measurements of particle locations

The location of a particle in the ice was expressed as the shortest distance between the particle and an ice grain boundary, and also that between the particle and an air-inclusion or PLI[22]. When there were multiple grain boundaries and/or air-inclusions or PLIs around the particle, the nearest ones were selected for the distance measurements. An OM image or a secondary electron image was analyzed using the image analysis software, Stream (Olympus Corporation) or Image J. The software allowed us to calculate the shortest distance between manually selected two points on the image, the center of a particle and a point on the grain boundary. Similarly, the shortest distance between the center of a particle and the outline of an air-inclusion or PLI was measured. Since these distances were measured using the two-dimensional image, the measurement errors seemed to be mainly due to the sublimed ice thickness during the experiment (mostly several micrometers and up to tens of micrometers; see Sec. 3.2.).

3.5. Processing energy dispersive X-ray spectroscopy data

The characteristic X-ray peak(s) corresponding to a given element were identified in the EDS spectra. From each peak, it was possible to calculate the X-ray count, weight ratio, normalized weight ratio, and atomic ratio of the element using the AZtec® software. The K-line of the characteristic X-

rays was used for most elements, but the M-line was used for Au and Pt.

Before the EDS analyses of the NEEM ice-core samples, we performed EDS analyses of sample holders. The EDS spectra from the sample holders showed peaks corresponding to Au, Al, Cu, K, C, O, and Ni. In addition to these elements, peaks corresponding to Pt could originate from some of the holders which were coated with Pt prior to the present study.

To confirm that an elemental peak in the EDS spectrum was derived from the particle in the NEEM ice-core samples, we compared the element weight ratio with those from the surrounding ice. If the particle existed close to a hydrate, the EDS spectrum was compared with that obtained from the hydrate. In the EDS spectra of ice, the peak corresponding to O was always present and those corresponding to C and N were frequently present (Fig. 4(a)). The EDS spectra of hydrates included also O, C, N, and additional Ar peak. The O peak seemed to originate from H_2O and the C peak seemed to originate from the Tissue-Tek Optimum Cutting Temperature Compound (Sakura Finetek Japan, Co., Ltd, Tokyo, Japan) [35], which was used to fixing each specimen (see Sec. 3.1.). The N peak could originate from nitrogen gas in the SEM chamber or an antiseptic contained in the Tissue-Tek (personal communication with the supplier). In this work, O was excluded from consideration because the O peak originating from ice was very large and prevented meaningful analysis of the O peak from a particle. To judge whether the C, N, and Ar peaks originated from a particle, the normalized weight ratios of C, N, and Ar were calculated from 212 EDS spectra obtained for ice. If the normalized weight ratio of C, N, or Ar from a particle was more than twice as high as the maximum weight ratio in the 212 spectra of ice (4.6%, 11%, and 0.32% for C, N, and Ar, respectively), then it was assumed that the element was included in the particle. The mean normalized weight ratios for ice were 0.89%, 0.43%, and 0.00%, and their standard deviations were 0.43%, 0.81%, and 0.01% for C, N, and Ar, respectively. If peaks corresponding to elements other than C, N, O, or Ar appeared in the EDS spectra of the ice surrounding a particle (Fig. 4(b)), these elements were not considered as components of the particle, because it was difficult to judge whether the element truly originated from the particle.

To confirm that an elemental peak other than C, N, O, or Ar originated from the particle, we compared the weight ratio with its standard deviation. The standard deviation was calculated using the AZtec® software and represented the uncertainty associated with the X-ray count noise and the weight ratio calculation. We considered that the element was detected in the particle if its weight ratio was greater than three times its standard deviation. The elements that had smaller weight ratios were abandoned. After removing C, N, O, Ar, and abandoned elements, the atomic ratios were recalculated

for the remaining elements, and they are presented in the catalog together with the original atomic ratios.

4. Data Records

The data from this study consists of three files, Particle_catalog.pdf, Particle_list.xlsx, and EDS_data.xlsx (Table 2). These data have been deposited in the Arctic Data archive System (ADS) (see Data Citation). In these files, identification numbers (IDs) were assigned to the particles and their EDS spectra. The identification number of the ith particle was denoted as "P-i", and the jth EDS spectrum from Particle P-i was denoted as "Sp i-j." Here we provide the pdf-formatted catalog for analyzed particles to make their characteristics easily-visible, but we can also offer individual particle images upon requests from readers.

The particle catalog presents the sample ID and date of analysis, as well as the optical microscopic images and secondary electron images of the ice specimens containing particles. The particle locations are clearly seen in these images (Fig. 5). For some specimens, multiple images from different layers of the specimen are shown. Images of the same area captured at different magnifications are outlined using the same color and type of line. The enlarged secondary electron images are also displayed to show each particle's shape and outline. Next to these enlarged images, there is a table that shows the area-equivalent diameter, aspect ratio, distance from the nearest grain boundary, and distance from the nearest air-inclusion (bubble, hydrate) or PLI.

For particles selected for analysis of their constituent elements, the EDS results are presented on the subsequent pages (Fig. 5). The EDS analysis of the surrounding ice is shown below the EDS results for each particle. At the top of each subsequent catalog page, the position of the EDS analysis is indicated with a circle. Note that the size of the circle does not represent the size of the electron beam or the region where the X-rays were generated. In some cases, the secondary electron image shown was different from that on the previous page. The field of view and/or the particle's orientation and/or morphology sometimes changed during SEM or EDS analyses because of the drift of the electron beam, rotation of the particle, and frost deposition. When the electron beam drifted, the beam irradiation positions were indicated in the images taken before and after the analysis (e.g., P65 in 226-C-VI-1). For most cases, all positions of EDS analyses for a particle in a secondary electron image are presented. However, when many analyses were performed, it was not possible to show all the analyzed positions in one image, so they are presented over multiple catalog pages.

The EDS spectra are presented below the image showing the analyzed position. The horizontal

and vertical axes show the X-ray energy and the X-ray count, respectively. An enlarged spectrum is also shown, if necessary. If multiple characteristic X-ray peaks appeared close together, the types of characteristic X-ray lines were indicated in the enlarged spectrum based on the AZtec® database.

Following the EDS spectra, we present a table that provides the characteristic X-ray peak count and calculated weight and atomic ratios. The notations used therein are defined as follows:

Peak: Characteristic X-ray peak count calculated by the AZtec® software.

WR: Weight ratio calculated by the AZtec® software.

Norm. WR: Normalized weight ratio calculated by the AZtec® software.

AR: Atomic ratio calculated by the AZtec® software.

AR': Atomic ratio recalculated by the authors.

The standard deviations (std.) for the Peak, WR, and Norm. WR are also included. The elements were classified as one of two types based on the EDS analyses of all particles: "elements frequently found" and "other elements." The "elements frequently found" are shown on all EDS spectra obtained from particles, while the "other elements" are only shown when the peaks corresponding to these elements were observed. The color scheme for the element symbols is as follows:

Red: Elements that were considered to originate from particles (see Sec. 3.5.).

Black: Elements that were not considered to originate from particles, although the authors observed the peaks (see Sec. 3.5.).

Gray: Elements for which no peaks were observed.

Blue: Oxygen.

The atomic ratios of the red-colored elements other than C, N, and Ar (i.e., AR') were also calculated, and are displayed in a pie chart.

The results of EDS analysis of the ice surrounding particles are presented in the same way as for particles. The EDS spectra obtained from ice were labeled as "Ice-*k*."

Particle_list.xlsx gives the following information for each particle:

Particle ID: Particle identification number.

Sample ID: Sample identification number (defined in Table 1 and Fig. 1).

Area number: Area in the sample where the particle was found.

Diameter [micrometers]: Area-equivalent diameter of the particle (see Sec. 3.3.).

Aspect ratio: Ratio of the minor-axis length to the major-axis length of the area-equivalent ellipse (see Sec. 3.3.).

Distance from grain boundary [micrometers]: Distance between the particle and a grain boundary (see Sec. 3.4.).

Distance from air-inclusion or plate-like inclusion [micrometers]: Distance between the particle and an air-inclusion (bubble or hydrate) or a PLI (see Sec. 3.4.).

Type of size and shape measurement: Procedure by which the size and shape of the particle were measured (see Sec. 3.3. and Fig. 3).

α: A secondary electron image was binarized using the Image J software, and the particle outline was drawn using the Image J software.

β: A secondary electron image was binarized using the Python-OpenCV software, and the particle outline was drawn using the Image J software.

γ: The outline was drawn manually by the authors.

EDS analysis: Indication of whether the particle was analyzed by energy dispersive X-ray spectroscopy ("Yes" or "No").

EDS_data.xlsx consists of worksheets detailing characteristic X-ray peak counts, weight ratios, normalized weight ratios, atomic ratios, and recalculated atomic ratios of each EDS spectrum obtained from the observed particles (Table 2). In each worksheet, the following information is provided:

EDS spectrum ID: EDS spectrum identification number (defined above).

Particle ID: Particle identification number.

Sample ID: Sample identification number (defined in Table 1 and Fig. 1).

Elements **C** to **Ba**: Values of the characteristic X-ray peak count, weight ratio, normalized weight ratio, atomic ratio, and recalculated atomic ratio of each element.

Total: Summation of each value except for the characteristic X-ray peak count.

Elements **C_sigma** to **Ba_sigma**: Standard deviations of the characteristic X-ray peak count, weight ratio, and normalized weight ratio of each element (standard deviations of atomic ratio and recalculated atomic ratio were not calculated).
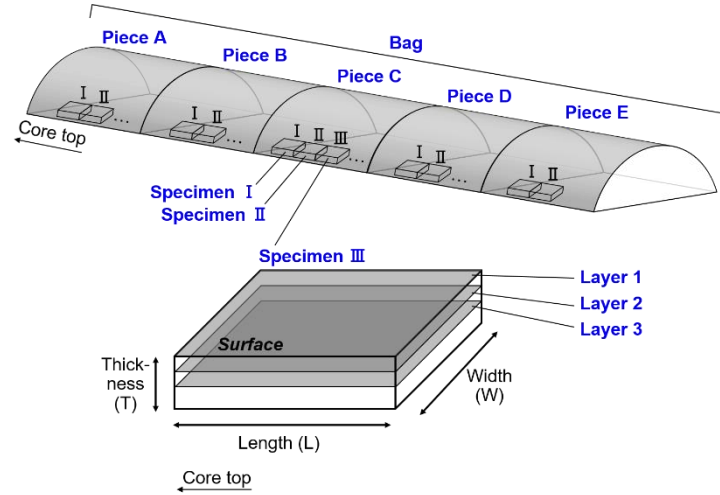
5. Figures

Fig. 1. Schematic diagram showing how the NEEM ice core specimens were cut, and an explanation of the labeling scheme for the Bag, Piece, Specimen, and Layer of the ice samples observed with optical and scanning electron microscopy.
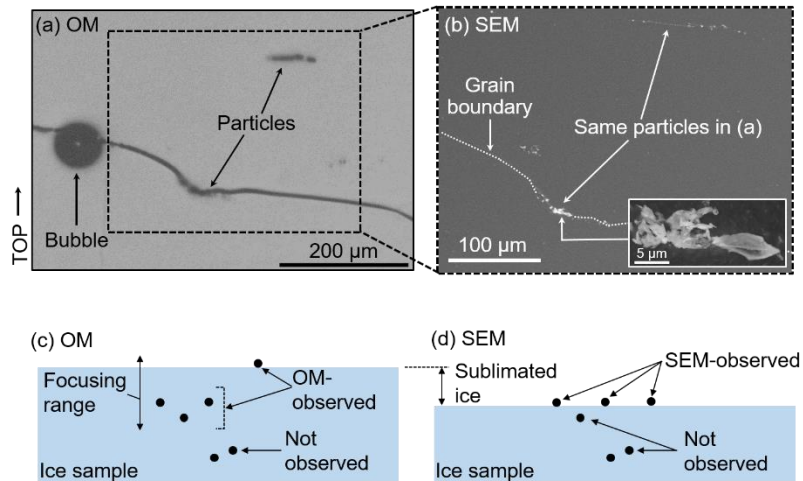

Fig. 2. Examples of (a) optical and (b) scanning electron microscopic images of ice and particles, along with schematic illustrations of cross-sections of the ice specimens observed with (c) optical microscopy and (d) scanning electron microscopy. The ice surface was sublimed mostly several micrometers, but sometimes up to several tens of micrometers after microtoming. The focusing range of optical microscopy of each objective lens was 6.1 μm, 18 μm, and 70 μm depending on the lenses (see main text). OM and SEM denote optical and scanning electron microscopy, respectively.
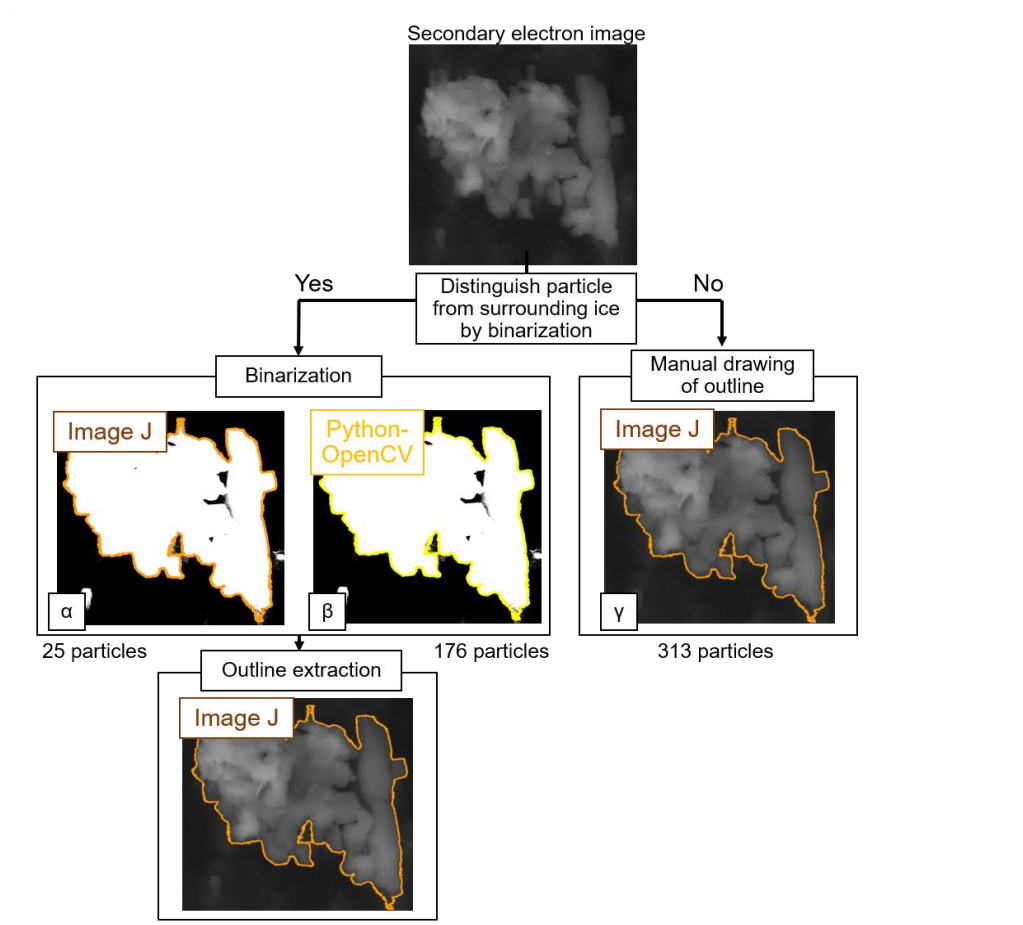
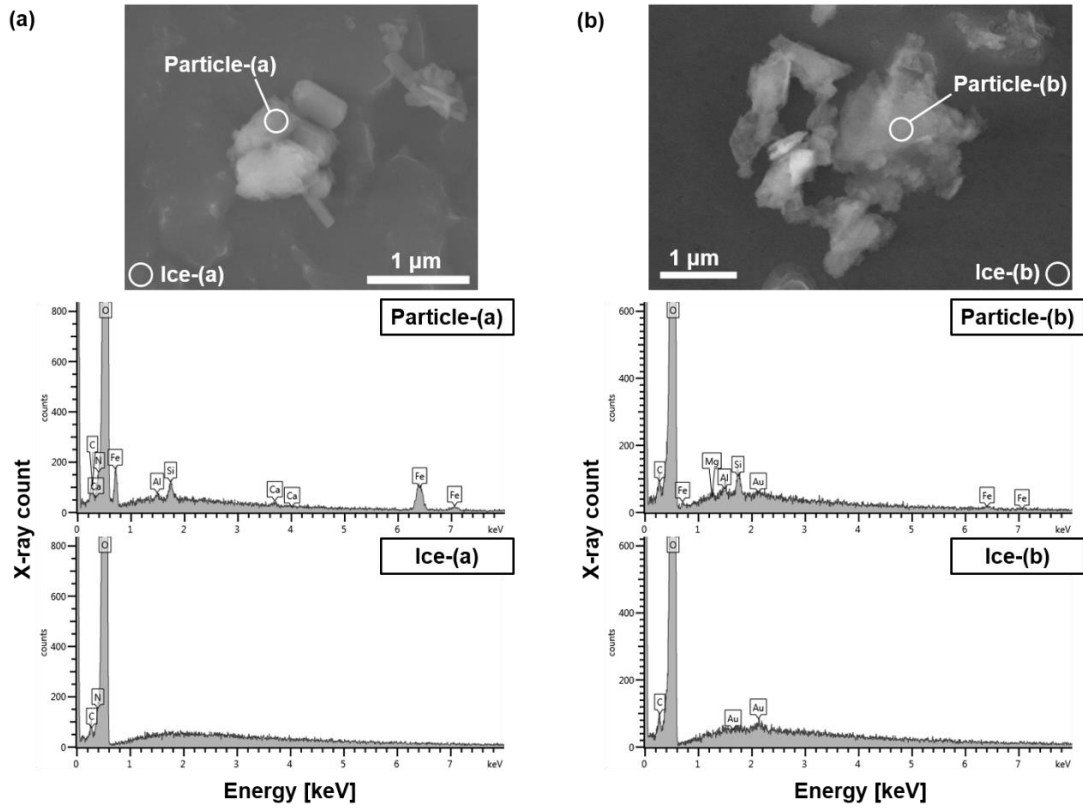Fig. 3.   Procedures of measurement of size and shape of a particle.

Fig. 4. Examples of secondary electron images of particles (top) and energy dispersive X-ray spectra from the particles and the surrounding ice (bottom). The spectra correspond to the positions indicated in the images. The EDS spectrum of the ice (labeled Ice-(a)) contains only the characteristic X-ray peaks of C, N and O; however, the EDS spectrum of ice shown in Ice-(b) also contains Au peaks, which is likely to originate from the sample holder. As explained in the main text, the spectroscopic data shown in particle (b) were excluded from Particle_catalog.pdf and EDS_data.xlsx.
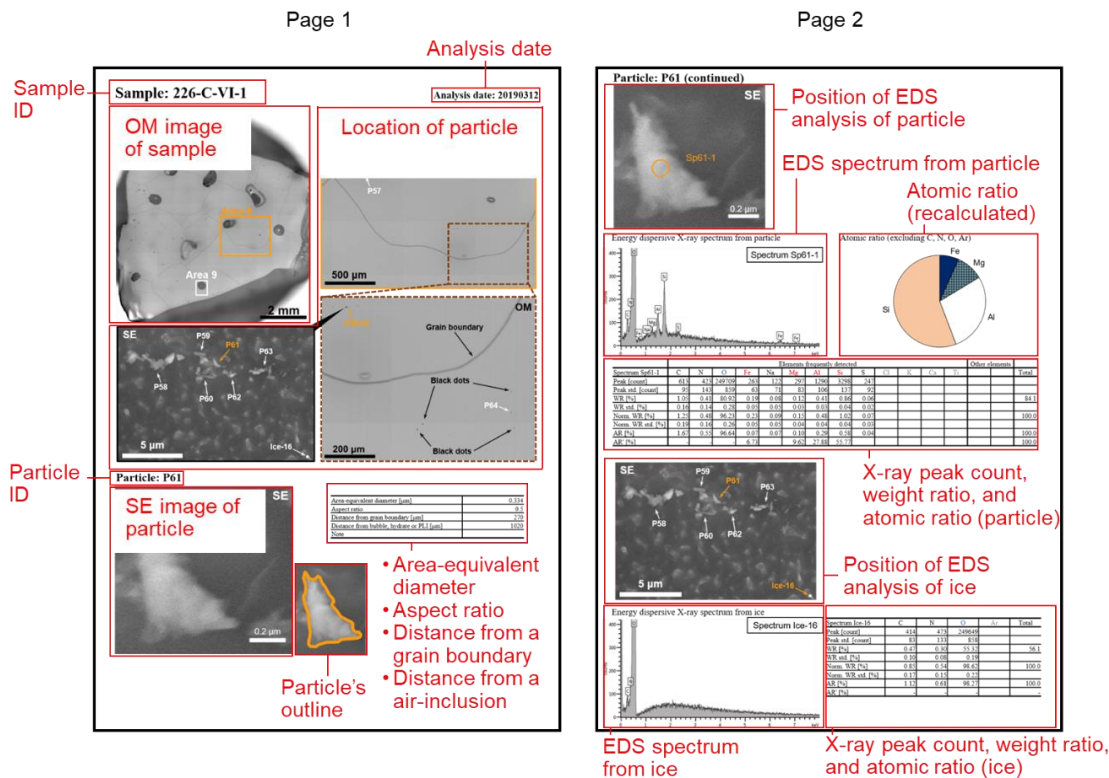
Fig. 5.　The contents and organization of the data catalog. The example pages contain energy dispersive X-ray spectroscopic analysis details.

6. Tables

Table 1. List of samples and particles.

Sample ID [i]	Depth [m]	Age covered by Bag [years before A.D. 2000] [ii]	Climate stage [ii]	Specimen Dimensions (L × W × T) [mm]	Area number [iii]	Number of observed particles in Layer	Particle ID	Corresponding page in the catalog	Analysis date (year-month-day)	Cloudy or clear band [iv]
226-C-I-1	123.934-123.941	458-460	Holocene	7 × 7 × 2	1	2	P1-P2	1	20190322	-
226-C-II-1	123.959-123.967			8 × 5 × 2	2	3	P3-P5	2-8	20190201	-
226-C-III-1	123.959-123.967			7 × 5 × 2	3	3	P6-P8	9-18	20190201	-
226-C-IV-1	123.993-124.005			12 × 9 × 2	4-5	46	P9-P54	19-91	20180502	-
226-C-V-1	123.999-124.008			9 × 9 × 2	6-7	2	P55-P56	92-94	20190315	-
226-C-VI-1	124.004-124.013			9 × 9 × 2	8-9	12	P57-P68	95-134	20190312	-
226-C-VII-1	124.004-124.018			11 × 9 × 2	10-11	9	P69-P77	135-162	20190318	-

2815-C-I-1	1548.022-1548.033			$9 \times 9 \times 4$	12-13	24	P78-P101	163-193	20170112	cloudy band
2815-C-I-2	1548.022-1548.033			$9 \times 9 \times 4$	14	30	P102-P131	194-210	20170323	cloudy band
2815-C-I-3	1548.022-1548.033			$9 \times 9 \times 4$	15	5	P132-P136	211-212	20180223	cloudy band
2815-C-II-1	1548.033-1548.045			$12 \times 11 \times 3$	16	2	P137-P138	213-219	20180330	clear layer
2815-C-III-1	1548.065-1548.075			$8 \times 9 \times 1$	17-18	14	P139-P152	220-226	20161013	clear layer
2815-C-III-2	1548.065-1548.075	19,126-19,170	The Last Glacial period (GS-2.1)	$8 \times 9 \times 1$	19	18	P153-P170	227-236	20180725	clear layer
2815-C-III-3	1548.065-1548.075			$8 \times 9 \times 1$	20-21	20	P171-P190	237-248	20180726	clear layer
2815-C-IV-1	1548.065-1548.075			$9 \times 6 \times 2$	22	5	P191-P195	249-260	20180720	clear layer
2815-C-V-1	1548.065-1548.075			$10 \times 7 \times 2$	23	3	P196-P198	261-262	20180718	clear layer
2815-C-V-2	1548.065-1548.075			$10 \times 7 \times 2$	24	15	P199-P213	263-280	20180727	clear layer
2815-D-I-1	1548.113-1548.126			$11 \times 7 \times 4$	25-27	33	P214-P246	281-326	20190412	clear layer

2815-D-II-1	1548.126-1548.133			$7 \times 10 \times 4$	28-30	22	P247- P268	327-369	20190424	cloudy band
2815-D-III-1	1548.135-1548.143			$8 \times 10 \times 4$	31-32	22	P269- P290	370-418	20190418	cloudy band
3575-E-I-1	1966.038-1966.048	62,015-62.134	The Last Glacial period (GS-18)	$9 \times 10 \times 4$	33-34	25	P291- P315	419-431	20191018	cloudy band
3575-E-II-1	1966.048-1966.054			$4 \times 11 \times 4$	35-36	10	P316-P325	432-436	20191024	cloudy band
3575-E-III-1	1966.054-1966.064			$9 \times 11 \times 4$	37-40	13	P326-P338	437-444	20191025	clear layer
3575-E-IV-1	1966.064-1966.073			$8 \times 11 \times 4$	41	40	P339-P378	445-473	20191101	clear layer
3575-E-V-1	1966.078-1966.084			$6 \times 10 \times 4$	42	17	P379-P395	474-483	20191031	cloudy band
3575-E-VI-1	1966.078-1966.086			$8 \times 10 \times 4$	43	22	P396-P417	484-495	20191105	cloudy band
3925-C-I-1	2158.356-2158.370	94,971-94,043	The Last Glacial period (GI-23.1)	$10 \times 10 \times 4$	44-45	2	P418-P419	496-499	20190813	-
3925-C-II-1	2158.356-2158.369			$9 \times 9 \times 4$	46	1	P420	500	20190925	-
3925-C-III-1	2158.366-2158.378			$8 \times 10 \times 4$	47-51	5	P421-P425	501-514	20190814	-

3925-C-IV-1	2158.365-2158.378			$9 \times 10 \times 4$	52-54	3	P426-P428	515-521	20190926	-
3925-C-V-1	2158.374-2158.388			$10 \times 9 \times 4$	55-57	4	P429-P432	522-528	20191004	-
3925-C-VI-1	2158.374-2158.389			$11 \times 10 \times 4$	58-62	7	P433-P439	529-548	20190830	-
3925-C-VII-1	2158.384-2158.398			$10 \times 11 \times 4$	63-67	9	P440-P448	549-565	20190927	-
3925-C-VIII-1	2158.394-2158.408			$10 \times 11 \times 4$	68-70	4	P449-P452	566-574	20191001	-
4375-A-I-1	2405.700-2405.709			$9 \times 9 \times 3$	71	1	P453	575-577	20190111	-
4375-A-II-1	2405.700-2405.709			$9 \times 9 \times 3$	72	8	P454-P461	578-582	20181116	-
4375-A-II-2	2405.700-2405.709	125,431-125,515	Eemian	$9 \times 9 \times 3$	73-74	2	P462-P463	583-587	20181228	-
4375-A-III-1	2405.715-2405.725			$9 \times 9 \times 3$	75-76	2	P464-P465	588-591	20181114	-
4375-A-IV-1	2405.725-2405.735			$9 \times 10 \times 3$	77	1	P466	592	20181109	-
4375-A-V-1	2405.735-2405.746			$10 \times 10 \times 3$	78-79	6	P467-P472	593-616	20190118	-

4375-A-VI-1	2405.735-2405.746			$10 \times 9 \times 3$	80	1	P473	617	20190128	-
4375-A-VI-2	2405.735-2405.746			$10 \times 9 \times 3$	81	1	P474	618	20190131	-
4375-A-VII-1	2405.746-2405.757			$9 \times 10 \times 3$	82-83	2	P475-P476	619-627	20190125	-
4375-B-I-1	2405.868-2405.881			$8 \times 10 \times 3$	84	1	P477	628	20190205	-
4375-B-I-2	2405.868-2405.881			$8 \times 10 \times 3$	85-87	6	P478-P483	629-644	20190308	-
4375-B-II-1	2405.878-2405.891			$10 \times 8 \times 3$	88-89	5	P484-P488	645-657	20190205	-
4375-B-II-2	2405.878-2405.891			$10 \times 9 \times 3$	90-92	26	P489-P514	658-716	20190208	-

Notes:

i. The sample identification number (ID) was defined by the Bag number, Piece number, Specimen number, and Layer number in that order (Fig. 1).

ii. The ages covered by a Bag and its corresponding climate stages are based on Rasmussen *et al.*[36] and NEEM community members[30]. For the Last Glacial period, Greenland Stadial (GS) and Greenland Interstadial (GI) climate conditions were also assigned from the ages based on Rasmussen *et al.*[37]

iii. Area where the particles were located in the specimen.

iv. In ice from the last glacial period, cloudy bands are often observed. A cloudy band is a light-scattering ice stratum that can be distinguished visually from adjacent clear strata[38], which is defined a clear layer.

Table 2. Description of archived particle data.

File name	Content
Particle_catalog.pdf	A catalog of analyzed particles that shows optical and scanning electron microscopic images of ice specimens and particles. It also presents the area-equivalent diameter of each particle, its distance from the nearest grain boundary and its distance from the nearest air-inclusion (bubble or hydrate) or plate-like inclusion and its energy dispersive X-ray spectra together with the EDS spectra of the surrounding ice. The graphical explanation is shown in Fig. 5.
Particle_list.xlsx	List of analyzed particles that also provides the area-equivalent diameter and aspect ratio of each particle, its distance from the nearest grain boundary, and its distance from the nearest air-inclusion (bubble or hydrate) or plate-like inclusion. The type of size and shape measurements (see Sec. 3.3.) are also shown.
EDS_data.xlsx	Numerical data from energy dispersive X-ray spectra obtained from particles. The file contains the following worksheets: 1. Peak – Characteristic X-ray peak counts of each element calculated by the AZtec® software. 2. WR – Weight ratio of each element calculated by the AZtec® software. 3. Norm. WR – Normalized weight ratio of each element calculated by the AZtec® software. 4. AR – Atomic ratio of each element calculated by the AZtec® software. 5. AR'_recalculated (denoted as AR' in Particle_catalog.pdf) – Atomic ratio of each element whose weight ratio was larger than three times its standard deviation (except C, N, O, and Ar), calculated by the authors (see Sec. 3.5.).

Author Contributions

W. Shigeyama, F. Nakazawa, K. Goto-Azuma, and N. Azuma designed the study. W. Shigeyama, T. Homma, N. Nagatsuka, R. V. Mateiu, M. Takata, and K. Goto-Azuma developed the technique for SEM/EDS analysis of ice samples. D. Dahl-Jensen and N. Azuma recovered the NEEM ice core. W. Shigeyama performed the particle analyses and data processing, and made the catalog. W. Shigeyama, K. Goto-Azuma, and F. Nakazawa led the manuscript preparation. All co-authors contributed to improve the manuscript.

Acknowledgments

References

1. Saruya, T. *et al*. Effects of microparticles on deformation and microstructural evolution of fine-grained ice. Journal of Glaciology. 2019, 65 (252), p. 531–541. https://doi.org/10.1017/jog.2019.29.

2. Song, M., Baker, I. and Cole, D. M. The effect of particles on creep rate and microstructures of granular ice. Journal of Glaciology. 2008, 54 (186), p. 533–537. https://doi.org/10.3189/002214308785836959.

3. Dahl-Jensen, D. and Gundestrup, N. S. Constitutive properties of ice at Dye 3, Greenland. The Physical Basis of Ice Sheet Modelling (Proceedings of the Vancouver Symposium, August 1987). IAHS Publ. no. 170. 1987, p. 31–43.

4. Paterson, W. S. B. Why ice-age ice is sometimes "soft". Cold Regions Science and Technology. 1991, 20 (1), p. 75–98. https://doi.org/10.1016/0165-232X(91)90058-O.

5.   Delmonte, B. *et al.* Aeolian dust in the Talos Dome ice core (East Antarctica, Pacific/Ross Sea sector): Victoria Land versus remote sources over the last two climate cycles. Journal of Quaternary Science. 2010, 25 (8), p. 1327–1337. https://doi.org/10.1002/jqs.1418.

6.   Delmonte, B., Petit, J. and Maggi, V. Glacial to Holocene implications of the new 27000-year dust record from the EPICA Dome C (East Antarctica) ice core. Climate Dynamics. 2002, 18, p. 647–660. https://doi.org/10.1007/s00382-001-0193-9.

7.   Lambert, F. *et al.* Dust-climate couplings over the past 800,000 years from the EPICA Dome C ice core. Nature. 2008, 452, p. 616–619. https://doi.org/10.1038/nature06763.

8.   Oyabu, I. *et al*. Chemical compositions of solid particles present in the Greenland NEEM ice core over the last 110,000 years. Journal of Geophysical Research: Atmospheres. 2015, 120 (18), p. 9789–9813. https://doi.org/10.1002/2015jd023290.

9.   Sakurai, T. *et al.* The chemical forms of water-soluble microparticles preserved in the Antarctic ice sheet during Termination I. Journal of Glaciology. 2011, 57 (206), p. 1027–1032. https://doi.org/10.3189/002214311798843403.

10.   Simonsen, M. F. *et al*. East Greenland ice core dust record reveals timing of Greenland ice sheet advance and retreat. Nature Communications. 2019, 10 (4494), p. 1–8. https://doi.org/10.1038/s41467-019-12546-2.

11.   Lambert, F. *et al*. The role of mineral-dust aerosols in polar temperature amplification. Nature Climate Change. 2013, 3, p. 487–491. https://doi.org/10.1038/nclimate1785.

12.   Ohgaito, R. *et al.* Effect of high dust amount on surface temperature during the Last Glacial Maximum: a modelling study using MIROC-ESM. Climate of the Past. 2018, 14 (11), p. 1565–1581. https://doi.org/10.5194/cp-14-1565-2018.

13.   Lambert, F. *et al.* Dust fluxes and iron fertilization in Holocene and Last Glacial Maximum climates. Geophysical Research Letters. 2015, 42 (14), p. 6014–6023. https://doi.org/10.1002/2015GL064250.

14.   Steffensen, J. P. The size distribution of microparticles from selected segments of the Greenland Ice Core Project ice core representing different climatic periods. Journal of Geophysical Research: Oceans. 1997, 102 (C12), p. 26755–26763. https://doi.org/10.1029/97JC01490.

15.   Ruth, U. *et al*. High-resolution microparticle profiles at NorthGRIP, Greenland: case studies of the calcium-dust relationship. Annals of Glaciology. 2002, 35 , p. 237–242. https://doi.org/10.3189/172756402781817347.

16.   De Angelis, M., Steffensen, J. P., Legrand, M., Clausen, and H. Hammer, C. Primary aerosol (sea

salt and soil dust) deposited in Greenland ice during the last climatic cycle: Comparison with east Antarctic records. Journal of Geophysical Research: Oceans. 1997, 102 (C12), p. 26681–26698. https://doi.org/10.1029/97JC01298.

17. Legrand, M. and Mayewski, P. Glaciochemistry of polar ice cores: A review. Reviews of Geophysics. 1997, 35 (3), p. 219–243. https://doi.org/10.1029/96RG03527.

18. Goto-Azuma, K. *et al*. Reduced marine phytoplankton sulphur emissions in the Southern Ocean during the past seven glacials. Nature Communications. 2019, 10, 3247. https://doi.org/10.1038/s41467-019-11128-6.

19. Alley, R. B., Perepezko, J. H. and Bentley, C. R. Grain growth in polar ice: I. Theory. Journal of Glaciology. 1986, 32 (112), p. 415–424.

20. Nes, E., Ryum, N. and Hunderi, O. On the Zener drag. Acta Metallurgica. 1985, 33 (1), p. 11–22. https://doi.org/10.1016/0001-6160(85)90214-7.

21. Lipenkov, V. Y. Air bubbles and air-hydrate crystals in the Vostok ice core. Physics of Ice Core Records. 2000, p. 327–358.

22. Nedelcu, A. F., Faria, S. H. and Kuhs, W. F. Raman spectra of plate-like inclusions in the EPICA-DML (Antarctica) ice core. Journal of Glaciology. 2009, 55 (189), p. 183–184. https://doi.org/10.3189/002214309788609010.

23. Ohno, H., Lipenkov, V. Y. and Hondoh, T. Formation of air clathrate hydrates in polar ice sheets: heterogeneous nucleation induced by micro-inclusions. Journal of Glaciology. 2010, 56 (199), p. 917–921. https://doi.org/10.3189/002214310794457317.

24. Ohno, H., Igarashi, M. and Hondoh, T. Salt inclusions in polar ice core: Location and chemical form of water-soluble impurities. Earth and Planetary Science Letters. 2005, 232 (1–2), p. 171–178 , https://doi.org/10.1016/j.epsl.2005.01.001.

25. Eichler, J. *et al.* Location and distribution of micro-inclusions in the EDML and NEEM ice cores using optical microscopy and in situ Raman spectroscopy. The Cryosphere. 2017, 11 (3), p. 1075–1090. https://doi.org/10.5194/tc-11-1075-2017.

26. Eichler, J. *et al.* Impurity Analysis and Microstructure Along the Climatic Transition From MIS 6 Into 5e in the EDML Ice Core Using Cryo-Raman Microscopy. Frontiers in Earth Science. 2019, 7, 20. https://doi.org/10.3389/feart.2019.00020.

27. Barnes, P. R. F., Mulvaney, R., Robinson, K. & Wolff, E. W. Observations of polar ice from the Holocene and the glacial period using the scanning electron microscope. Annals of Glaciology. 2002,

35, p. 559–566. https://doi.org/10.3189/172756402781816735.

28.   Delmonte, B. *et al*. Dust size evidence for opposite regional atmospheric circulation changes over east Antarctica during the last climatic transition. Climate Dynamics. 2004, 23, p. 427–438. https://doi.org/10.1007/s00382-004-0450-9.

29.   Cullen, D. and Baker, I. Observation of impurities in ice. Microscopy Research and Technique. Special Issue: Functional Cytology of Nitric Acid in Striated Muscle—Part I. 2001, 55 (3), p. 198–207 , https://doi.org/10.1002/jemt.10000.

30.   NEEM community members. Eemian interglacial reconstructed from a Greenland folded ice core. Nature. 2013, 493, p. 489–494. https://doi.org/10.1038/nature11789.

31.   Barnes, P. R. F., Wolff, E. W., Mallard, D. C. and Mader, H. M. SEM studies of the morphology and chemistry of polar ice. Microscopy Research and Technique. 2003, 62 (1), p. 62–69, https://doi.org/10.1002/jemt.10385.

32.   Shigeyama, W. *et al*. Microstructural analysis of Greenland ice using a cryogenic scanning electron microscope equipped with an electron backscatter diffraction detector. Bulletin of Glaciological Research. 2019, 37, p. 31–45. https://doi.org/10.5331/BGR.19R01.

33.   Weikusat, I. *et al*. Cryogenic EBSD on ice: preserving a stable surface in a low pressure SEM. Journal of Microscopy. 2011, 242 (3), p. 295–310. https://doi.org/10.[11]11/j.1365-2818.2010.03471.x.

34.   Prior, D. J. *et al*. Making EBSD on water ice routine. Jounal of Microscopy. 2015, 259 (3), p. 237–256. https://doi.org/10.1111/jmi.12258.

35.   Sakura Finetek Japan. Safety Data Sheet of Tissue-Tek Optimum Cutting Temperature Compound. https://www.sakura-finetek.com/ja/customer-support/Safety-data-sheets (accessed 2021-06-27).

36.   Rasmussen, S. O. *et al*. A first chronology for the North Greenland Eemian Ice Drilling (NEEM) ice core. Climate of the past. 2013, 9, p. 2713–2730, https://doi.org/10.5194/cp-9-2713-2013.

37.   Rasmussen, S. O. *et al*. A stratigraphic framework for abrupt climatic changes during the Last Glacial period based on three synchronized Greenland ice-core records: refining and extending the INTIMATE event stratigraphy. Quaternary Science Reviews. 2014, 106 p. 14–28. https://doi.org/10.1016/j.quascirev.2014.09.007.

38.   Svensson, A. *et al*. Visual stratigraphy of the North Greenland Ice Core Project (NorthGRIP) ice core during the last glacial period. Journal of Geophysical Research: Atmospheres. 2005, 110 (D02108). https://doi.org/10.1029/2004JD005134.

Data Citation

Shigeyama, W., Nakazawa, F., Goto-Azuma, K., Homma, T., Nagatsuka, N., Mateiu, R., Takata, M., Azuma, N. and Dahl-Jensen, D. Microparticles in a deep ice core drilled at NEEM, Greenland: cryogenic scanning electron microscopic observations of location, size, shape, and constituent elements. 2.00, Japan, Arctic Data archive System (ADS), 2021. https://doi.org/10.17592/001.2021031801.
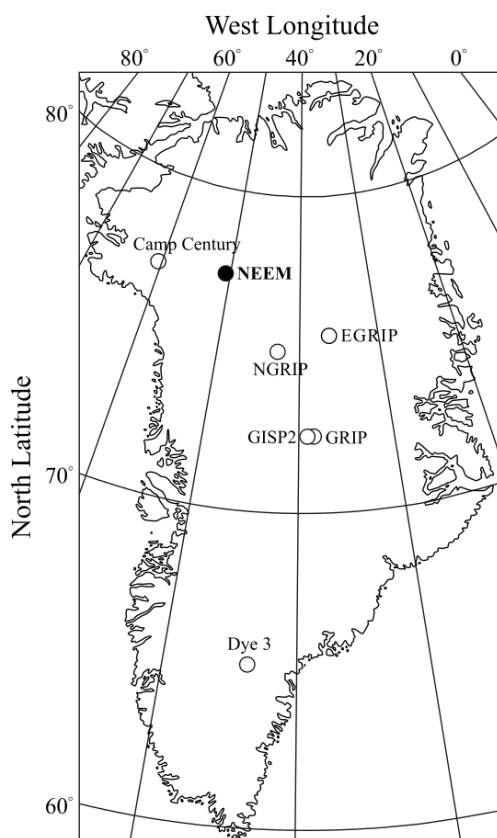
Supplemental figure

Fig. S1. Location of the drilling site of the North Greenland Eemian Ice Drilling (NEEM) project (filled circle). Locations of other deep ice-coring sites are also indicated with open circles: Camp Century, GRIP (Greenland Ice Core Project), GISP2 (Greenland Ice Sheet Project 2), NGRIP (North Greenland Ice Core Project), EGRIP (East Greenland Ice Core Project), and Dye 3.